Chemical imaging of tissue *in vivo* with video-rate coherent anti-Stokes Raman scattering microscopy

Conor L. Evans*, Eric O. Potma*†, Mehron Puoris'haag‡, Daniel Côté‡, Charles P. Lin‡§, and X. Sunney Xie*§

*Department of Chemistry and Chemical Biology, Harvard University, 12 Oxford Street, Cambridge, MA 02138; and ‡Wellman Center for Photomedicine, Massachusetts General Hospital, 55 Fruit Street, Boston, MA 02114

Communicated by William Klemperer, Harvard University, Cambridge, MA, September 22, 2005 (received for review August 18, 2005)

Imaging living organisms with molecular selectivity typically requires the introduction of specific labels. Many applications in biology and medicine, however, would significantly benefit from a noninvasive imaging technique that circumvents such exogenous probes. *In vivo* microscopy based on vibrational spectroscopic contrast offers a unique approach for visualizing tissue architecture with molecular specificity. We have developed a sensitive technique for vibrational imaging of tissues by combining coherent anti-Stokes Raman scattering (CARS) with video-rate microscopy. Backscattering of the intense forward-propagating CARS radiation in tissue gives rise to a strong epi-CARS signal that makes *in vivo* imaging possible. This substantially large signal allows for real-time monitoring of dynamic processes, such as the diffusion of chemical compounds, in tissues. By tuning into the CH_2 stretching vibrational band, we demonstrate CARS imaging and spectroscopy of lipid-rich tissue structures in the skin of a live mouse, including sebaceous glands, corneocytes, and adipocytes, with unprecedented contrast at subcellular resolution.

nonlinear microscopy | vibrational imaging | back scattering

Optical microscopy is unique among current imaging modalities in its ability to probe living tissue with subcellular resolution, enabling the visualization of morphological details in tissue that cannot be resolved by ultrasound or magnetic resonance imaging. To date, however, optical microscopy has not been completely successful in providing high-resolution morphological information with chemical specificity. The contrast in confocal reflectance microscopy (1) and optical coherence tomography (2), for instance, is based on refractive index differences and cannot directly probe the chemical composition of tissue structures. Fluorescence microscopy, while extremely sensitive and widely used, is limited in chemical selectivity by the small number of intrinsic fluorophores, such as NAD(P)H, riboflavins, and elastin (3, 4). The introduction of extrinsic fluorophores provides specific probes, but often causes unwanted perturbations. Second harmonic generation microscopy is useful for visualizing well ordered protein assemblies, such as collagen fibers, but has inadequate sensitivity and specificity for other tissue components (4, 5).

Vibrational spectra of biological specimens contain a multitude of molecular signatures that can be used for identifying biochemical constituents in tissue. Conventional vibrational microscopy methods, however, lack the sensitivity required for rapid tissue examination. Infrared microscopy is limited by low spatial resolution caused by the long wavelength of infrared light (6), as well as strong water absorption in biological specimens. Raman microspectroscopy, while capable of discriminating healthy from diseased tissue *in vivo* (7), is hampered by long integration times and/or high laser powers that are not desirable in biomedical applications.

Much stronger vibrational signals can be attained with coherent anti-Stokes Raman scattering (CARS), a nonlinear Raman technique (8). CARS makes use of two laser beams, a pump beam at frequency ω_p and a Stokes beam at frequency ω_S (Fig. 1). When the beat frequency ($\omega_p - \omega_S$) matches the frequency of a particular Raman active molecular vibration (ω_{vib}), the resonant oscillators are coherently driven, resulting in a strong anti-Stokes signal at $\omega_{as} = 2\omega_p - \omega_S$. Typical CARS signals from submicrometer objects are orders of magnitude stronger than the corresponding spontaneous Raman response. Because CARS is a nonlinear effect, the signal is generated only at the laser focus, which allows for point-by-point 3D imaging of thick specimens, similar to two-photon fluorescence microscopy (9).

Recent developments in laser sources and detection schemes have significantly improved the capabilities of CARS as a biological imaging modality (10). CARS microscopy has proven useful for mapping lipid compartments (11), protein clusters (12), and water distributions (13) in cell tissue cultures. Current state-of-the-art CARS microscopes have high enough sensitivity to detect single lipid bilayers (14, 15). Recent work on tissue slices has shown the potential for CARS as a tool for tissue imaging (16). The strongest CARS signals are usually collected in transmission mode, but live tissue imaging necessitates detection in the backward (epi-) direction. It has been shown that epi-CARS is sensitive to subwavelength structures, whereas larger-sized structures are rendered invisible in this detection mode (17). It was initially thought that this size-selective imaging property of epi-CARS microscopy would preclude its use for imaging tissues, which contain many structures with dimensions larger than a wavelength. In this work, we demonstrate that, in tissue, linear backscattering of the forward-generated CARS signal gives rise to a strong epi-CARS signal.

This strong signal allows us to obtain video-rate CARS in live skin tissues with an unprecedented speed, revealing vivid contrast of skin structures in a nonperturbative way. This work signifies the potential of CARS microscopy for biomedical applications.

Methods

Laser Light Source. We have achieved CARS video-rate imaging of live tissues by selecting a light source and microscope design that produce strong vibrational signals under benign excitation conditions (Fig. 1). Linear absorption and photodamage are minimized by using near infrared excitation. We use a 1,064-nm mode-locked Nd:vanadate laser with 10-W output power from High-Q Laser (Hohenems, Austria). The laser delivers a stable 7-ps, 76-MHz pulse train through semiconductor saturable absorber mirror mode-locking. A portion of the output (10%) is split off and used as the CARS Stokes beam. The remaining 9 W is used for synchronously pumping an optical parametric oscillator (Levante, APE, Berlin) to generate the CARS pump beam. The optical parametric oscillator (OPO) is equipped with a periodically poled KTP crystal comprised of different periodic

Conflict of interest statement: No conflicts declared.

Abbreviations: CARS, coherent anti-Stokes Raman scattering; DiD, $C_{67}H_{103}ClN_2O_3S$.

†Present address: Department of Chemistry, University of California, Irvine, CA 92697.

§To whom correspondence may be addressed. E-mail: lin@helix.mgh.harvard.edu or xie@chemistry.harvard.edu.

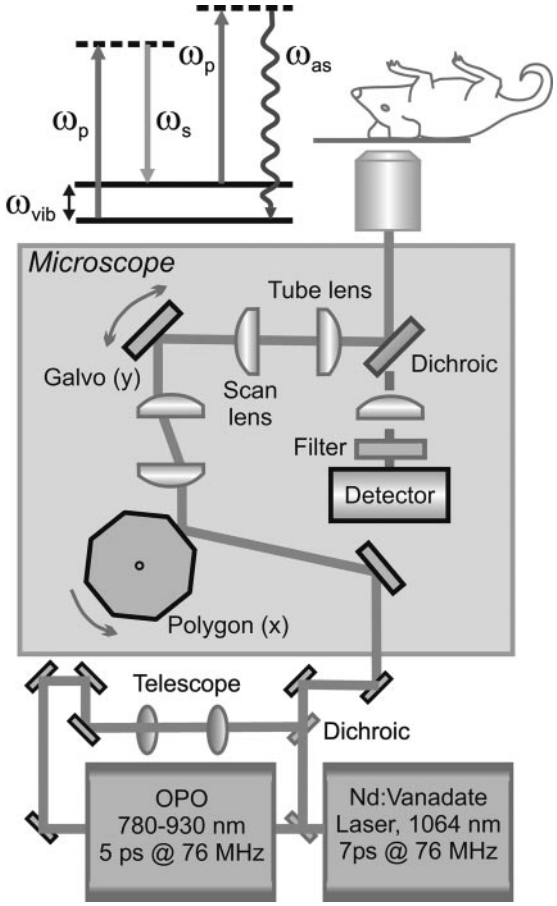

Fig. 1. Schematic of the real-time CARS imaging microscope, based on a mode-locked Nd:vanadate picosecond laser and a tunable synchronously pumped optical parametric oscillator (OPO). Temporal overlap of the pump and Stokes pulse trains is controlled with an optical delay stage. A fast rotating polygon mirror provides rapid beam scanning in the x-direction, while a synchronized galvanometric mirror scans the beam along the *y* axis. A 1.2 numerical aperture water immersion lens is used for focusing the beams. Maximum power at the sample is 50 mW for each beam. Signals detected with a red-sensitive photomultiplier tube are processed by a computer and displayed at video rate on a monitor for real-time inspection of the tissue. (*Inset*) The CARS energy diagram with pump (ω_p) and Stokes (ω_s) excitation frequencies, the blue-shifted anti-Stokes (ω_{as}) signal frequency, and the vibrational frequency (ω_{vib}) is shown.

grating zones that allow for temperature-controlled wavelength tuning over four separate intervals covering the 1,560- to 1,860-nm range. The OPO signal is intracavity doubled to produce tunable radiation between 780 and 930 nm with output powers of ≈1.5 W at 76 MHz. The narrow bandwidth pulses (≈3.5 cm^{-1}) with durations of 5 ps assure a sufficient spectral resolution and a high signal-to-background ratio (18). This light source provides excellent power stability and intrinsic synchronization of the pump and Stokes pulse trains, which are essential for high-sensitivity video-rate imaging.

The divergence of the CARS pump and Stokes beams is controlled by a telescope in each beam path. The CARS pump is passed through a delay stage for adjustment of the temporal overlap of the two pulse trains. The beams are collinearly combined on a dichroic mirror (z950bc, Chroma Technology, Brattleboro, VT) and directed to the video-rate microscope. The average power of each beam at the sample is attenuated to <50 mW to avoid photodamage of the tissue sample.

The Video-Rate Microscope. The video-rate microscope is based on a modified confocal scan head for real-time imaging (Vivascope, Lucid, Henrietta, NY) (1). CARS images are obtained by raster scanning the collinear pump and Stokes pulses over the sample and collecting the generated anti-Stokes light. Rapid scanning in the x-direction is provided by a rotating polygon mirror (Lincoln Laser, Phoenix), while a galvanometric mirror (General Scanning, Watertown, MA) scans the y-dimension (slow axis). Twenty frames are acquired per s with short pixel dwell times (0.16 μs) to minimize local heating of the sample by linear absorption. The overlapped pump and Stokes beams are focused to a diffraction limited volume in the sample by a 1.2 numerical aperture water immersion objective lens (×60, IR UPlanApo, Olympus, Melville, NJ), yielding a CARS resolution of 0.3 μm in the lateral plane and 1.5 μm in the axial direction. The objective lens is combined with a 40-mm focal length tube lens to achieve high-resolution imaging over a wide field of view (800 × 600 μm). The microscope is configured as an inverted microscope for convenient handling of the animal. A manually adjustable 3D sample stage provides additional flexibility for selecting areas of interest in the tissue. Epi-CARS signals are separated from the incident radiation with a short-wave pass dichroic mirror (z750sx, Chroma Technology) and filtered through three bandpass filters centered around the anti-Stokes wavelength (35–5107, Ealing, Rocklin, CA). A red-sensitive photomultiplier tube (R3896, Hamamatsu, Bridgewater, NJ) is used as the photodetector in close vicinity of the dichroic mirror. The signal is digitized by a digital conversion board (NI-1408, National Instruments, Austin, TX) and sent to a computer for image processing.

Sample Handling. Female mice (BALB/c or SKH-1 hairless, Charles River Breeding Laboratories) were anesthetized with Ketamine (80 mg/kg)/Xylazine (12 mg/kg) i.p. and placed on the stage of the inverted microscope. The mouse ear was flattened with methylcellulose gel (Methocel 2%, Novartis Pharma, Nürnberg, Germany) on a borosilicate coverslip, using a cotton tip. Imaging was performed at room temperature in sessions typically lasting 1 h. The intralipid solution used as a tissue model was purchased from Sigma and diluted to a 10% emulsion. Mineral oil used in the diffusion studies was Johnson & Johnson (New Brunswick, NJ) baby oil.

Red blood cells were labeled with DiD ($C_{67}H_{103}ClN_2O_3S$, Molecular Probes) for combined CARS and two-photon imaging. Red blood cells were isolated from fresh whole human blood by using density gradient centrifugation (Histopaque density gradient, Sigma). To keep the red blood cells at physiologic concentration (5 × 10^9 per ml), the isolated red blood cells were resuspended in a suitable volume of PBS. A 0.1-ml volume of red blood cell suspension was then mixed with 0.9 ml of RPMI cell media 1640 and incubated with 0.1 ml of 1 mM Vybrant DiD for 30 min at 37°C to arrive at a final DiD concentration of ≈0.1 mM. Excess dye was washed by centrifuging the cells at 400 × *g* for 6 min two to three times. Washed cells were resuspended in 1 ml of RPMI medium 1640. For the experiment, 0.2 ml of the final washed suspension was injected into the tail vein of the mouse.

***Ex Vivo* Raman Spectroscopy.** Mouse ears were frozen and cut along the transversal direction into 10-μm slices with a microtome (UCT cryo-ultramicrotome, Leica Microsystems, Bannockburn, IL) equipped with a glass knife. The tissue slices were then transferred to a coverslip and immersed in aqueous buffer for microscopic examination. Raman spectra were taken on a Raman microspectrometer (Labram, Horiba, Jobin Yvon, Edison, NJ). Spectra from individual sebaceous glands and adipocytes, identified through transmission light microscopy, were recorded with a high numerical aperture objective (×60, 1.2 numerical aperture, IR UPlanApo, Olympus) by using 15 mW of

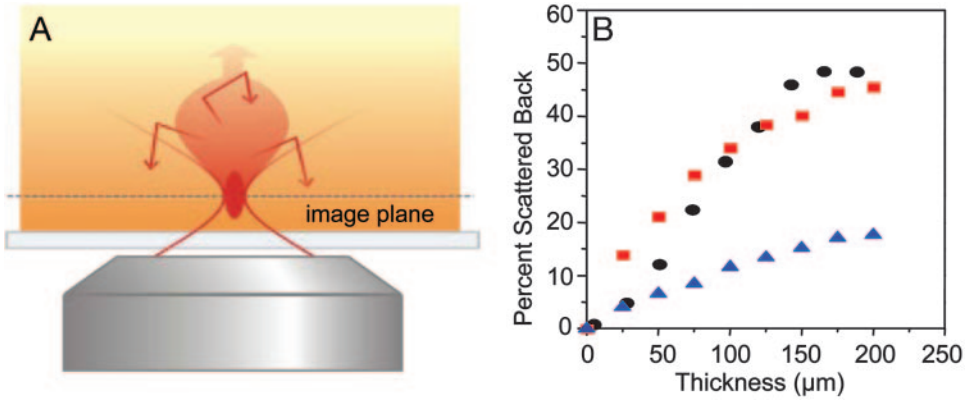

Fig. 2. Epi-CARS signal contrast arises from the backscattering of forward propagating photons generated in focus. (*A*) Schematic of the scattering mechanism responsible for the contrast in epi-CARS from thick tissues. Part of the forward propagating signal is backscattered. (*B*) Collection efficiency of epi-detection of the forward propagating signal as a function of sample thickness for tissue phantom (10% intralipid suspension) and mouse skin tissue. The focal volume was placed 1 μm deep in the tissue phantom for both measurements and calculations. Measurements are indicated by black dots, and Monte Carlo simulations of photon backscattering are indicated by the red squares. The experimental ratio was determined by normalizing the epi-detected signal from the tissue phantoms to forward-collected signal generated from water under the same excitation conditions. For the simulations, a scattering coefficient μ_s of 400 cm^{-1}, a tissue absorption coefficient μ_a of 0.01 cm^{-1}, and a scattering anisotropy g of 0.75 was used for intralipid (21). The blue triangles indicate the calculated results obtained for mouse skin tissue with $\mu_s = 150$ cm^{-1}, $\mu_a = 0.1$ cm^{-1}, and $g = 0.85$. More than 15% of the forward-generated CARS photons in mouse tissue are backscattered and collected by the objective.

laser radiation at 632.8 nm. The spectra were integrated for 30 s and averaged over five individual recordings.

Numerical Simulations. Simulations for backscattering of CARS photons were performed with the Monte Carlo technique (19) and are presented in detail in *Supporting Text*, which is published as supporting information on the PNAS web site.

Results

Backscattering Is the Primary Reason for Strong Epi-CARS Signals from Tissue. The epi-CARS signals observed from the tissue are very strong. It is known that intense signals are generated in the forward direction because of phase matching, whereas the epi-signal is severely suppressed because of destructive interference of the CARS waves (17). It has been demonstrated that epi-signals can be detected only when the destructive interference in the backward direction is incomplete. This incomplete interference occurs when (*i*) CARS waves are generated by subwavelength objects or (*ii*) when a CARS response is induced at the interface between two materials (17). Neither of these mechanisms, however, can account for the intensity and contrast observed in our epi-CARS tissue images. Not only is the signal from tissue simply too strong to originate from these mechanisms, but 3D scans of tissues reveal objects much larger than the focal volume.

We propose a mechanism for epi-CARS detection in (thick) tissues based on light scattering in turbid media (20, 21). The strong epi-CARS signal arises because a significant portion of the forward propagating signal, which is generated at the focus, is redirected backward by multiple scattering events in tissue (Fig. 2*A*).

To validate and quantify this mechanism for CARS tissue imaging, we collected epi-CARS signals from a tissue model system (10% intralipid emulsion) (22) as a function of the sample thickness (Fig. 2*B*). The epi-CARS signal increases with the thickness of the scattering layer above the focal plane, proving that the detected signal is dominated by backscattering of initially forward propagating CARS. This observation is supported by our Monte Carlo simulations. We calculated that, in mouse skin tissue, >15% of the forward-propagating CARS is scattered back and collected by the objective lens. This contribution is the dominant source of contrast because the forward CARS signal is usually orders of magnitude stronger than the epi-CARS signal that arises solely from incomplete destructive interference (17). We believe that this scattering mechanism may play an important role in second harmonic generation microscopy in tissue as well, because the forward-generated second harmonic generation is readily backscattered.

The high backscattering efficiency from thick samples (>150 μm) (Fig. 2*B*) indicates that the scattering volume is rather large. As a result, the scattering efficiency is virtually invariant as the focal spot is scanned across the sample because the large scattering volume averages out spatial inhomogeneity. We stress that, despite the large scattering volume, the nonlinear CARS signal only originates from the laser focal spot. As the focal spot size defines the spatial resolution, backscattering of the forward propagating signal does not change the 3D resolution and sectioning capability of CARS microscopy.

CARS Tissue Imaging. We used the CARS microscope to image mouse ear tissue *in vivo*. Fig. 3 shows CARS tissue images taken at the 2,845-cm^{-1} symmetric stretch vibration of lipids at various depths. A ubiquitous component of the skin, lipids are abundant in CH_2 bonds, and therefore exhibit a strong and distinct signature in the CARS spectrum. At the skin surface, a bright polygonal pattern outlines the corneocytes of the stratum corneum (Fig. 3*A*), which arises from the intercellular space rich in lipids, ceramides, and cholesterol (23). At 20–40 μm from the skin surface, sebaceous glands are clearly visible (Fig. 3*B*). These multicellular compartments are packed with small, micrometer-sized sebum reservoirs containing CH_2-rich triglycerides and wax esters (24). The nuclei of the sebum-producing cells can be recognized as dark holes (Fig. 3*C*). Large, fat-producing adipocytes are found 60–80 μm deep in the dermis (Fig. 3*D*), often aligned along blood vessels. At the same depth, fibrous structures are occasionally discerned in the vicinity of blood vessels, which could possibly be CH-rich myelinated nerve bundles (16). The subcutaneous layer, composed of smaller adipocytes 20–30 μm in size, can be seen at depths of ≈100 μm (Fig. 3*E*).

When the Raman shift was tuned off-resonance, only a weak (<5%) nonresonant CARS signal remained. The feebleness of this nonresonant signal demonstrates that the contrast at 2,845 cm^{-1} originates primarily from the on-resonant lipid contribution. If the pump and Stokes pulses were temporally offset, the

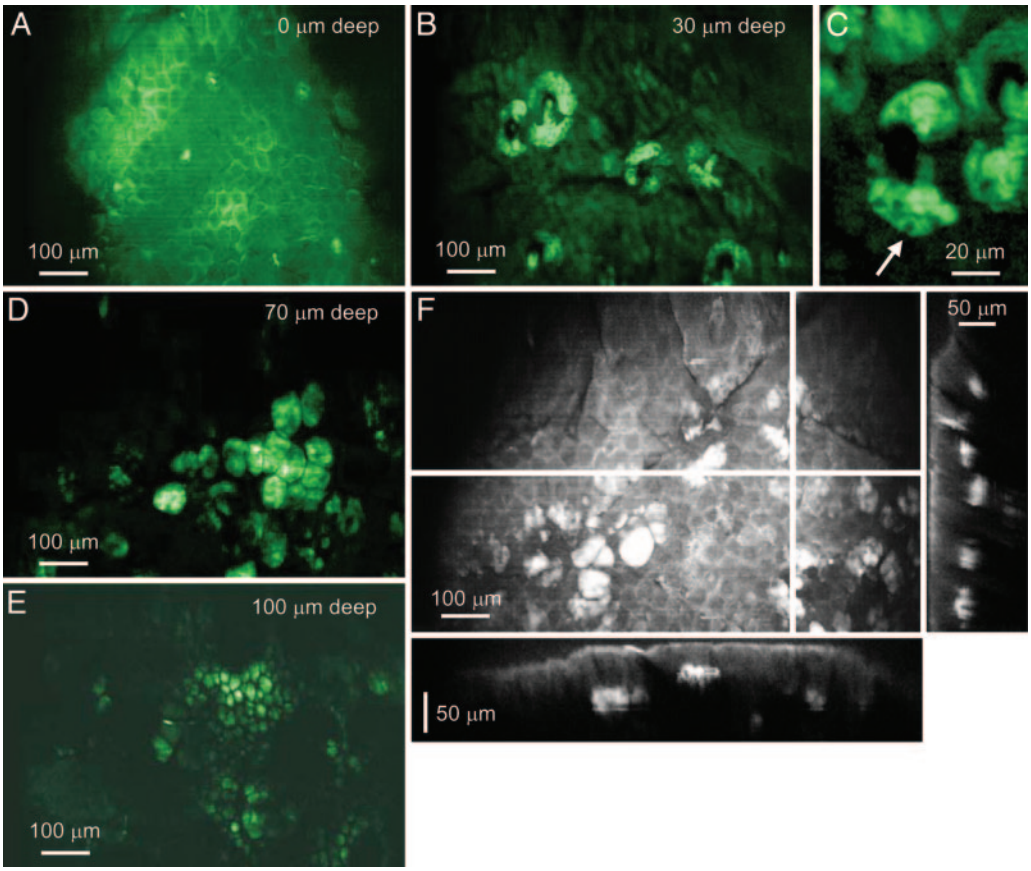

Fig. 3. Images of a hairless mouse ear. The Raman shift is set at 2,845 cm^{-1} (ω_p = 816.8 nm) to address the lipid CH_2 symmetric stretch vibration. The frames are averaged for 2 s. (*A*) Stratum corneum with bright signals from the lamellar lipid intercellular space that surrounds the polygonal corneocytes. Bright punctuated dots are ducts of sebaceous glands. (*B*) Sebaceous glands at ≈30 μm from skin surface. (*C*) Individual cells of the gland compartment can be recognized, with nuclei visible as dark holes (arrow). (*D*) Adipocytes of the dermis at ≈60 μm from skin surface. (*E*) Adipocytes of the subcutaneous layer at a depth of ≈100 μm. (*F*) 2D projection of 60 depth-resolved slices separated by 2 μm. Panels to the right and under *F* show the *yz* and *xz* cross sections taken at the white lines, respectively.

signal vanished, which rules out any significant contributions from two-photon-induced autofluorescence.

Because the CARS signal is generated only at the focal point, video-rate imaging allows for the rapid construction of 3D tissue maps. This 3D imaging capability is illustrated in Fig. 3*F*, a 2D overlap composed of 60 depth-resolved slices separated by 2 μm. The stratum corneum is clearly visible in the cross-sectional CARS images at the surface along with bright sebaceous glands and adipocytes deeper in the tissue. The cross-section images appear similar to tomographic maps obtained with optical coherence tomography (OCT), but unlike OCT arise from chemical contrast and offer higher lateral spatial resolution.

CARS microscopy can also be readily combined with two-photon fluorescence microscopy *in vivo* to provide additional information. Fig. 4 shows a combined CARS and two-photon fluorescence image of mouse skin taken at a depth of 20 μm. A percentage of red blood cells has been labeled with DiD to highlight the capillary network. The spatial interplay between the blood vessels and sebaceous glands is apparent as the capillaries branch and loop around the tissue structures.

The video-rate imaging speed of the CARS microscope allows rapid inspection of live tissue in real time. Movie 1, which is published as supporting information on the PNAS web site, explores different depths of the mouse skin and demonstrates the high contrast obtainable at video rate.

CARS Offers Chemical Selectivity. CARS can differentiate tissue structures based on their respective chemical composition. In the range of 2,800–2,900 cm^{-1}, the CARS spectra of the sebaceous glands and the deeper lying adipocytes are nearly identical (Fig. 5*A*). In the region of 2,900–2,970 cm^{-1}, however, the signal from the sebaceous glands is weak, whereas a strong signal from the adipocytes remains. As a result, CARS contrast of sebaceous glands and adipocytes at Raman shifts 2,845 and 2,956 cm^{-1} are significantly different (Fig. 5 *C*–*F*).

The CH vibrational region (2,800–3,100 cm^{-1}) is composed of

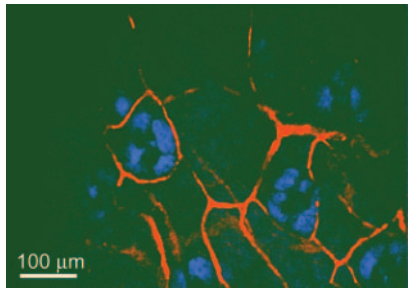

Fig. 4. A combined sequential CARS and two-photon fluorescence tissue image. The CARS signal is colored blue, and the two-photon fluorescence is colored red. The Raman shift is set to 2,845 cm^{-1}, with the 816.7-nm pump beam driving two-photon fluorescence excitation of the injected DiD dye. The sebaceous glands can be seen within the branched and looped capillary network.

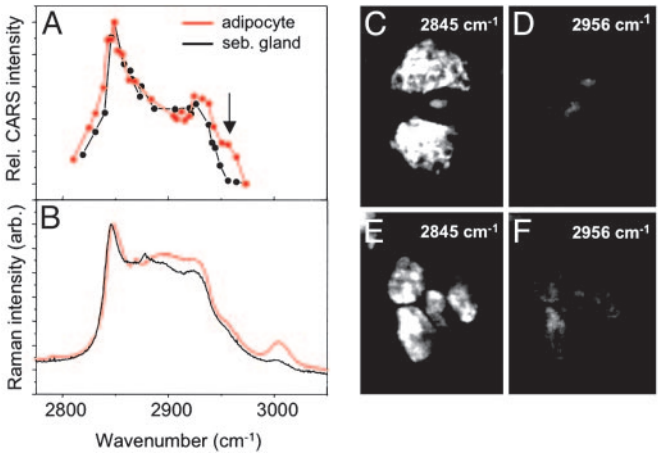

Fig. 5. Spectral differences between sebaceous glands and dermal adipocytes. (*A*) *In vivo* CARS spectrum of sebaceous gland (black) and adipocyte (red) obtained by point-by-point wavelength scanning of the pump beam. Note the dissimilarity in spectral intensity at higher wavenumbers (2,956 cm^{-1}, indicated by arrow), caused by the different chemical lipid composition. (*B*) *Ex vivo* Raman spectrum of individual sebaceous glands (black) and adipocytes (red) recorded from 10-μm-thick microtomed tissue sections. We note that the CARS spectrum in the 2,900- to 2,970-cm^{-1} range offers more spectral sensitivity to the degree of saturation of aliphatic chains than the spontaneous Raman spectrum. (*C* and *D*) CARS image of a sebaceous gland at 2,845 cm^{-1} (*C*) and 2,956 cm^{-1} (*D*). (*E* and *F*) CARS image of adipocytes at 2,845 cm^{-1} (*E*) and 2,956 cm^{-1} (*F*).

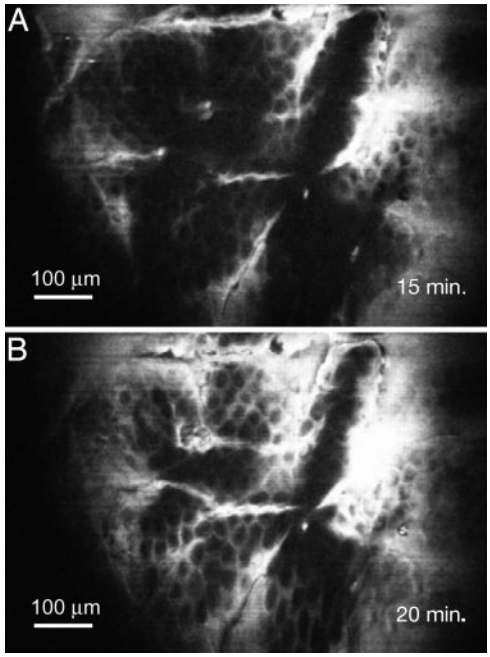

Fig. 6. Diffusion of mineral oil through mouse epidermis. (*A*) Externally applied mineral oil penetrates the stratum corneum through the lipid clefts between corneocytes. Image was taken ≈20 μm below the surface 15 min after application of the oil. Raman shift is set to 2,845 cm^{-1}, yielding a bright signal from the oil. (*B*) The same area is shown 5 min later. Brighter signal indicates a higher oil concentration caused by time-dependent diffusion, which can be clearly seen during the 5-min time window.

many vibrational bands, including the aliphatic CH_2 and the vinyl CH stretches. Therefore, the spectral shape is indicative of chemical composition. Sebum, composed mostly of trigylcerides and other saturated fats, should have a large CARS signal at the symmetric CH_2 stretching frequency, near 2,845 cm^{-1}. As adipocytes contain a higher concentration of unsaturated fatty acids than sebaceous glands, the change in the CARS spectrum reflects the difference in chemical composition.

To verify this result, mouse ears were microtomed to make 10-μm-thin tissue slices that could be probed in a Raman microscope. *Ex vivo* Raman spectra of individual sebaceous glands and adipocytes support our assignment (Fig. 5*B*). The increased spectral intensity of the adipocytes relative to the sebaceous glands in the 2,870- to 2,940-cm^{-1} of the Raman spectrum causes the high-frequency dip of the CARS spectrum to shift to higher energy, accounting for the difference in the CARS contrast. Therefore, even within the range of the CH stretching region, CARS can selectively highlight different chemical compositions.

CARS Microscopy Can Track Chemical Diffusion in Skin. The unique imaging properties of the CARS microscope make it possible to follow in real time the delivery of specific chemicals in tissue *in vivo*. To demonstrate this potential, we visualized the penetration of externally applied mineral oil through the superficial layers of the mouse skin. Changes in the distribution of the oil can be observed by tuning into the oil's CH_2 stretching vibration.

After application, the mineral oil was found to penetrate through the stratum corneum by passing through the lipid domains between the corneocytes (Fig. 6). Over a time span of 20 min, the concentration of oil in the stratum corneum clearly rose. We did not see an increased CARS signal in the dermis, indicating that the oil penetrated no further than the epidermal layer.

Discussion

Over the past several years, the capability of CARS imaging has vastly improved through a combination of laser engineering and microscope optimization. While a forward-CARS image took 30 min to collect in 1999 (25), we have demonstrated here the ability to collect images at a rate of 30 per s in the epi-direction, an improvement of nearly five orders of magnitude in sensitivity. This high sensitivity of epi-detected CARS microscopy has made it possible to study tissues *in vivo* with vibrational selectivity.

CARS microscopy is well suited for studying lipid distributions in tissue. Lipids and fats are heterogeneously distributed in tissue, being stored in select cellular environments and organs. This heterogeneity, combined with the high sensitivity of CARS microscopy to CH vibrational modes, makes CARS the ideal choice to study lipid and fat distributions *in vivo* in real time. With further improvements in detection sensitivity we expect that real-time imaging with vibrational contrast from protein and DNA will be within reach. The DNA and protein Raman responses are far weaker than that of lipid and require an increase of at least an order of magnitude in sensitivity. Emerging methods offer the prospect of increased sensitivity that will bring CARS imaging to the next level (26).

One of the main concerns regarding tissue imaging is the ability to probe deep into the sample. The ultimate penetration depth is limited by the working distance of the microscope objective. In this study, the maximum penetration depth in mouse skin was found to be working distance limited to 125 μm, which is comparable to depths reached with two-photon-excited fluorescence by using the same objective. The practical penetration depth of near-IR radiation is most likely affected by the distortion of the focal volume and the reduction of power at the focus caused by linear scattering of the incoming light in turbid tissue. Penetration depths as large as a few millimeters have been achieved in two-photon fluorescence microscopy by using long working distance objectives (27, 28). We expect the CARS probe depth to increase when using such

objectives. In addition, the penetration depth can be further increased by using longer wavelengths for CARS excitation to reduce the amount of scattering experienced in the turbid tissue environment.

In collecting the CARS images, we used illumination doses of 20 W/cm^2 on nonpigmented skin (50 mW per beam), which is much lower than the photodamage threshold of 500 W/cm^2 for continuous wave radiation found for pigmented skin (29). Although nonlinear photodamage caused by high pulse peak power is a concern, we have not observed any indication of such an effect in the tissue. We note that the picosecond pulse train has a lower peak power than that of femtosecond pulse trains used in two-photon fluorescence tissue imaging (3).

In vivo CARS microscopy adds chemical selectivity to real-time noninvasive optical histology and may prove useful for tissue pathology. In addition, epi-detected CARS can be combined with fiber-optic endoscopy for applications such as molecular imaging of intravascular atherosclerotic plaques and real-time guiding of surgical interventions.

We thank Dr. David Bell for help with tissue sectioning. This research was funded by the National Institutes of Health, the National Science Foundation, the Department of Defense Medical Free Electron Program, and in particular the National Institutes of Health Director's Pioneer Award (to X.S.X.). C.L.E. was supported by a National Science Foundation Graduate Research Fellowship.

1. Rajadhyaksha, M., Gonzalez, S., Zavislan, J. M., Anderson, R. R. & Webb, R. H. (1999) *J. Invest. Dermatol.* **113,** 293–303.
2. Fujimoto, J. G. (2003) *Nat. Biotechnol.* **21,** 1361–1367.
3. Masters, B. R. & So, P. T. C. (2001) *Opt. Express* **8,** 2–10.
4. Zipfel, W. R., Williams, R. M., Christie, R., Nikitin, A. Y., Hyman, B. T. & Webb, W. W. (2003) *Proc. Natl. Acad. Sci. USA* **100,** 7075–7080.
5. Campagnola, P. J. & Loew, L. M. (2003) *Nat. Biotechnol.* **21,** 1356–1360.
6. Miller, L. M., Smith, G. D. & Carr, G. L. (2003) *Biol. Phys.* **29,** 219–230.
7. Choo-Smith, L. P., Edwards, H. G. M., Endtz, H. P., Kros, J. M., Heule, F., Barr, H., Robinson, J. S., Bruining, H. A. & Puppels, G. J. (2002) *Biopolymers* **67,** 1–9.
8. Maker, P. D. & Terhune, R. W. (1965) *Phys. Rev.* **137,** A801–A818.
9. Denk, W., Strickler, J. H. & Webb, W. W. (1990) *Science* **248,** 73–76.
10. Cheng, J. X. & Xie, X. S. (2004) *J. Phys. Chem. B* **108,** 827–840.
11. Nan, X. L., Cheng, J. X. & Xie, X. S. (2003) *J. Lipid Res.* **44,** 2202–2208.
12. Cheng, J. X., Book, L. D. & Xie, X. S. (2001) *Opt. Lett.* **26,** 1341–1343.
13. Potma, E. O., de Boeij, W. P., van Haastert, P. J. M. & Wiersma, D. A. (2001) *Proc. Natl. Acad. Sci. USA* **98,** 1577–1582.
14. Potma, E. O. & Xie, X. S. (2003) *J. Raman Spectrosc.* **34,** 642–650.
15. Wurpel, G. W. H., Schins, J. M. & Muller, M. (2004) *J. Phys. Chem. B* **108,** 3400–3403.
16. Wang, H., Fu, Y., Zickmund, P., Shi, R. & Cheng, J. X. (2005) *Biophys. J.* **89,** 581–591.
17. Cheng, J. X., Volkmer, A. & Xie, X. S. (2002) *J. Opt. Soc. Am. B* **19,** 1363–1375.
18. Cheng, J. X., Volkmer, A., Book, L. D. & Xie, X. S. (2002) *J. Phys. Chem. B* **106,** 8493–8498.
19. Wang, L., Jacques, S. L. & Zheng, L. (1995) *Comput. Meth. Prog. Biomed.* **47,** 131–146.
20. Yodh, A. G., Tromberg, B., Sevick-Muraca, E. & Pine, D., eds. (1997) *J. Opt. Soc. Am. A* **14,** 136–342.
21. Bonner, R. F., Nossal, R., Havlin, S. & Weiss, G. H. (1987) *J. Opt. Soc. Am. A* **4,** 423–432.
22. Flock, S. T., Jacques, S. L., Wilson, B. C., Star, W. M. & van Gemert, M. J. (1992) *Lasers Surg. Med.* **12,** 510–519.
23. Wertz, P. W., Schwartzendruber, D. C., Madison, K. C. & Downing, D. T. (1987) *J. Invest. Dermatol.* **89,** 419–425.
24. Stewart, M. E. & Downing, D. T. (1991) *Adv. Lipid Res.* **24,** 263–301.
25. Zumbusch, A., Holtom, G. & Xie, X. S. (1999) *Phys. Rev. Lett.* **82,** 4142–4145.
26. Potma, E. O., Evans, C. L. & Xie, X. S. (2005) *Opt. Lett.*, in press.
27. Beaurepaire, E., Oheim, M. & Mertz, J. (2001) *Optics Comm.* **188,** 25–29.
28. Cahalan, M. D., Parker, I., Wei, S. H. & Miller, M. J. (2002) *Nat. Rev. Immunol.* **2,** 872–880.
29. Rajadhyaksha, M., Anderson, R. R. & Webb, R. H. (1999) *Appl. Opt.* **38,** 2105–2115.